ACCSCIENCE PUBLISHING

Journal of Seismic Exploration

ARTICLE

Reducing interpretation risks in organic-rich low-velocity mudstone using rock physics modeling in Yinggehai Basin, South China Sea

Yanhua Xie, Jinpeng Li*, Fang Li, Wanyuan Sun, and Yayun Dang

Department of Geophysics, Research Institute, China National Offshore Oil Corporation Limited Hainan Branch, Haikou, Hainan, China

(This article belongs to the *Special Issue: Geophysical Inversion and Intelligent Prediction Technologies for Complex Hydrocarbon Reservoirs*)

Abstract

The mudstone in a specific exploration area of the Yinggehai Basin is rich in organic matter and serves as a paradigmatic example of a low-velocity mudstone formation in rock physics. This type of interval exhibits seismic response characteristics similar to those of hydrocarbon reservoirs, which complicates the identification of gas reservoirs and the prediction of gas-bearing zones in this area. In this study, the analysis and modeling of rock physical characteristics within the exploration area are investigated. Based on the actual drilling curve and coring analysis data, a rock physics model of the low-velocity mudstone reservoir is established using self-consistent approximations and the Ciz–Gassmann model, and the influence of organic matter content on the mudstone's elastic properties is analyzed. Additionally, a robust quantitative inversion procedure is introduced to test the feasibility of inverting for porosity, clay content, and water saturation to mitigate the risk of low-velocity mudstone. The application of actual data, including core samples, logging data, and seismic database, demonstrates the effectiveness of this method and provides technical support for seismic prediction of sand body identification and hydrocarbon detection.

Keywords: Low-velocity mudstone; Rock physics; Hydrocarbon detection; Total organic carbon; Seismic interpretation

***Corresponding author:**
Jinpeng Li
(lijp40@cnooc.com.cn)

Citation: Xie Y, Li J, Li F, Sun W, Dang Y. Reducing interpretation risks in organic-rich low-velocity mudstone using rock physics modeling in Yinggehai Basin, South China Sea. *J Seismic Explor.* 2026;35(2):025460110. doi: 10.36922/JSE025460110

Received: November 14, 2025

Revised: February 2, 2026

Accepted: February 5, 2026

Published online: April 30, 2026

Copyright: © 2026 Author(s). This is an Open-Access article distributed under the terms of the Creative Commons Attribution License, permitting distribution, and reproduction in any medium, provided the original work is properly cited.

Publisher's Note: AccScience Publishing remains neutral with regard to jurisdictional claims in published maps and institutional affiliations.

1. Introduction

The Yinggehai Basin is located in the western part of the northern continental shelf of the South China Sea. Some gas reservoirs exhibit typical bright-spot seismic response characteristics of low frequency and strong amplitude[1–5], which is beneficial for target search. As exploration and development have progressed, the error rate of target search using strong amplitude characteristics in the Yinggehai Basin has gradually increased.[6–8] It can thus be concluded that the atypical reflection characteristics exhibited by low-frequency, strong-amplitude bright spots prior to drilling are not indicative of a response from gas-bearing sandstone (GS). Rather, these phenomena are frequently the result of false bright spots, which are often caused by lithology changes. A significant and archetypal

rationale pertains to the impact of low-velocity mudstone (LVM). There is no strict correspondence between proven gas reservoirs and strong seismic reflection characteristics. The issue of how to avoid LVM traps has become a pressing concern in exploration practice.[9,10]

Petrophysics bridges physical property parameters to elastic responses. The inverse problem in petrophysical modeling involves predicting reservoir parameters based on petrophysical models. The fundamental principle of this process involves the extraction of reservoir parameters from pre-stack seismic or elastic data. This process decouples different lithologic and physical property layers.[11] For instance, incorporating rock physics statistical patterns and prior information on physical properties into seismic forward-modeling objective functions enables inversion for porosity and impedance parameters.[12–14] Alternatively, establishing mappings between physical parameters and saturated rock velocities using equivalent medium theory and wave-induced fluid flow seismic wave dispersion equations enables the solution of inverted parameters within Bayesian pre-stack amplitude-variation-with-offset (AVO) inversion or elastic impedance inversion frameworks.[15,16] The existing body of research indicates that reservoir parameter extraction based on rock physics modeling is a reliable and effective method for reservoir prediction and hydrocarbon detection.[17,18]

Targeted research on petrophysical modeling and seismic prediction methods is essential to analyze the seismic petrophysical characteristics of LVM, clarify their petrophysical properties, mitigate associated risks, and enhance reservoir prediction and hydrocarbon detection success rates. The present study analyzes and summarizes the petrophysical characteristics of LVM encountered in a drilling area of the Yinggehai Basin, based on actual data from the western South China Sea exploration zone. For typical LVM formations with rich-type mechanisms, rock-physical modeling and analysis are conducted based on the equivalent-medium theory. The velocity inversion prediction is achieved using actual well data. The establishment of a quantitative seismic prediction methodology tailored for formations containing LVM represents an advancement in the field. This methodology provides a sound theoretical and methodological basis for reservoir prediction and hydrocarbon detection.

2. Geological setting

The Yinggehai Basin is located in the sea area to the east of the Indo–China Peninsula and to the west of Hainan Island. It includes first-order tectonic units, such as the central depression, Yingdong slope, and Yingxi slope.[1,2] The basin is characterized by Cenozoic overpressure and high temperature, and is considered to be a significant area for the exploration and development of natural gas resources in the South China Sea. Numerous large and medium-sized gas fields have been discovered and brought into production in the Yinggehai Basin. The location of the target area in the Yinggehai Basin is shown in Figure 1. The formation, environment, and petroleum source of this basin are shown in Figure 2. The sedimentary evolution of the Yinggehai Basin from the late Oligocene Lingshui Formation to the Miocene Yinggehai Formation has been shown to record a transition from late rifting to a depression and an accelerated subsidence period. The Lingshui Formation is deposited in the sea–land transition zone in a shallow-sea environment and developed multi-type reservoirs, including delta, shore-shallow sea sandstone, and carbonate platform reservoirs. The provenance is evident from northwest, west, and other directions, and the characteristics of sand–shale interbeds are clearly discernible.[3] The Yinggehai Formation has transitioned from a deep-sea to a semi-deep-sea environment, with the Red River as the dominant source. The formation of thick mudstones is widespread, and isolated deep-water turbidite sandstones are present, forming a natural gas accumulation system under high-temperature, high-pressure conditions. The presence of mud diapirs is identified as the primary control factor within this system. The evolution of this sedimentary sequence indicates the transformation of the basin from a rift-divided lake basin to a unified, rapidly subsiding basin. The sedimentary system is characterized by the predominance of gravity flow over traction flow. The reservoir gradually transformed from a horizontal, continuous layered reservoir to a lenticular lithologic body. This unique oil and gas geological model comprises a lower generation and an upper reservoir, with high temperatures and pressures, and diapir control within the basin.[7,8]

3. Data and methods

3.1. Data

Low-velocity mudstone is a geophysical relative concept, signifying that the P-wave velocity (V_p) of this particular mudstone is lower in comparison to that of its adjacent normal mudstone or sandy mudstone strata.[2,3] A significant decrease in velocity leads to the formation of a strong wave impedance interface between this type of mudstone and the high-speed formation below, and this characteristic will result in strong reflection amplitude on the seismic profile, which is a typical seismic characteristic of gas-bearing reservoirs. While performing geosteering during drilling operations, if strong seismic reflection amplitudes are the sole criterion for judgment, there is a risk of misidentifying the LVM layer as a valuable GS layer.[4,5] This can deviate the

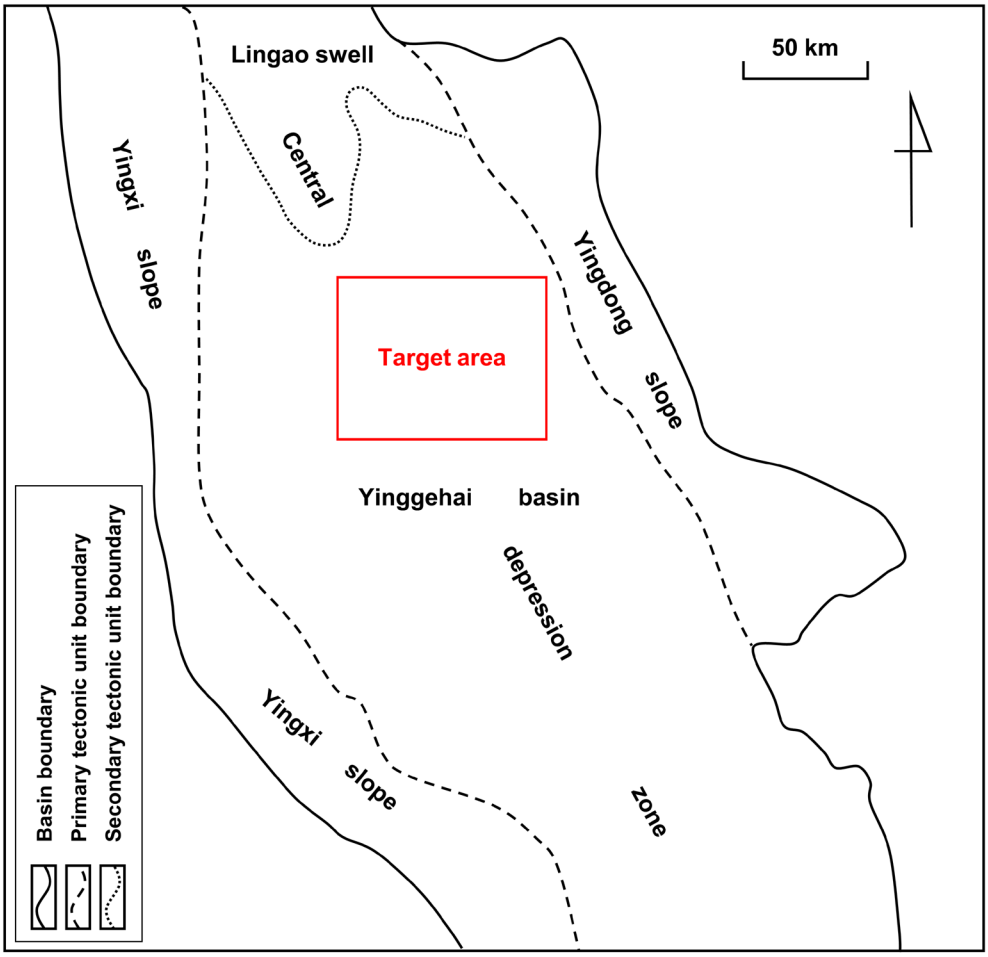

Figure 1. Location of the target area in the Yinggehai Basin

drilling trajectory from the actual target reservoir, leading to invalid footage and economic losses.[6]

Exploration practices suggest that the mechanisms that induce low-velocity characteristics in the region's mudstones include three factors: pore pressure (p) anomalies, effects of clay minerals, and organic matter content. Statistical data are presented in Table 1 and Figure 3. The first category of LVM exhibited primarily low resistivity (R_t), a high P- and S-wave velocity ratio (V_p/V_s), and a high pore pressure coefficient (p coefficient). However, its gamma ray (GR), total organic carbon (TOC), and gas-detected total hydrocarbon values were comparable to those of high-velocity background mudstone (BM). TOC content can represent the abundance of organic matter in rocks. This LVM's internal composition differs little from that of normal-velocity BM. The main distinction lies in the external environment, specifically a significantly higher p coefficient than that of the BM. The second category of LVM exhibited similar characteristics to the first category in terms of R_t, V_p/V_s, TOC, gas-detected total hydrocarbons, and R_t versus V_p. However, it showed significant differences in gamma curves, with GR values markedly higher than those of the normal-velocity mudstone background, while the p coefficient is comparable. This indicates that the pressure environment of this LVM is not substantially different from that of normal-velocity mudstone backgrounds, with the primary distinction being clay mineral content, which was markedly higher than that of normal-velocity mudstone backgrounds. The third category of LVM differed from the first and second categories. Although differences in GR, R_t, and the p coefficient were not pronounced compared to the normal-velocity BM, the third category of LVM showed markedly lower V_p/V_s and higher TOC, overall resembling the characteristics of gas-bearing strata. This LVM category showed minimal differences from BM in external temperature and pressure conditions and clay content, with the primary distinction in organic carbon content.

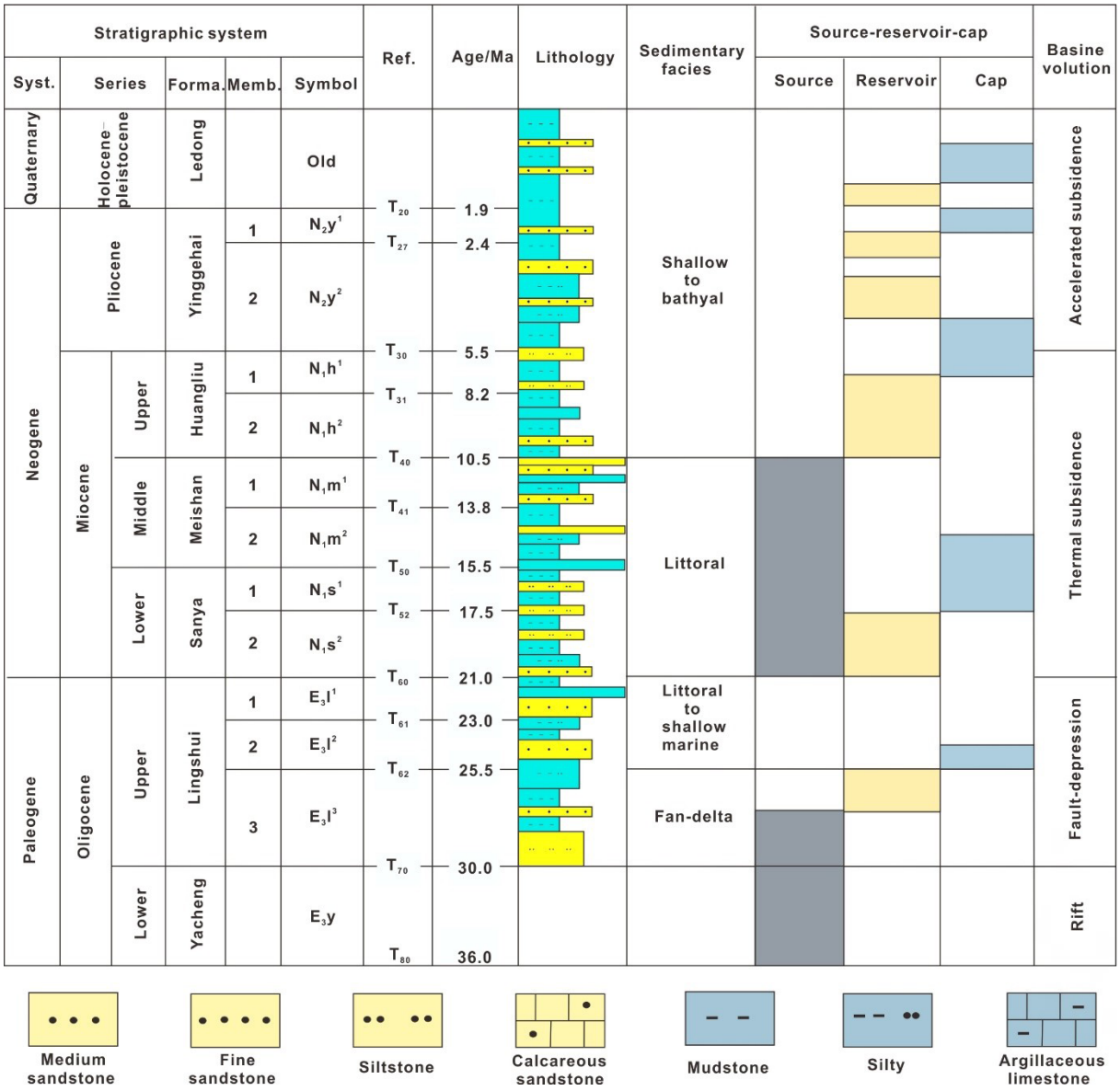

Figure 2. Formation, environment, and the petroleum source of the Yinggehai Basin

Table 1. Statistical table of geophysical characteristics of low-velocity mudstone in Yinggehai Basin

Layers	Parameter characteristics						Cause of low-velocity
	Resistivity	GR	V_p/V_s	TOC	Pore pressure coefficient	Gas detection, total hydrocarbon	
Category 1	Low	Similar	High	No	High	Similar	High pressure
Category 2	Low	High	High	No	Similar	Similar	Massive clay
Category 3	High/similar	High/similar	Low/similar	Yes	Similar	High	High TOC

Abbreviations: GR: Gamma ray; TOC: Total organic carbon; V_p/V_s: P- and S-wave velocity ratio.

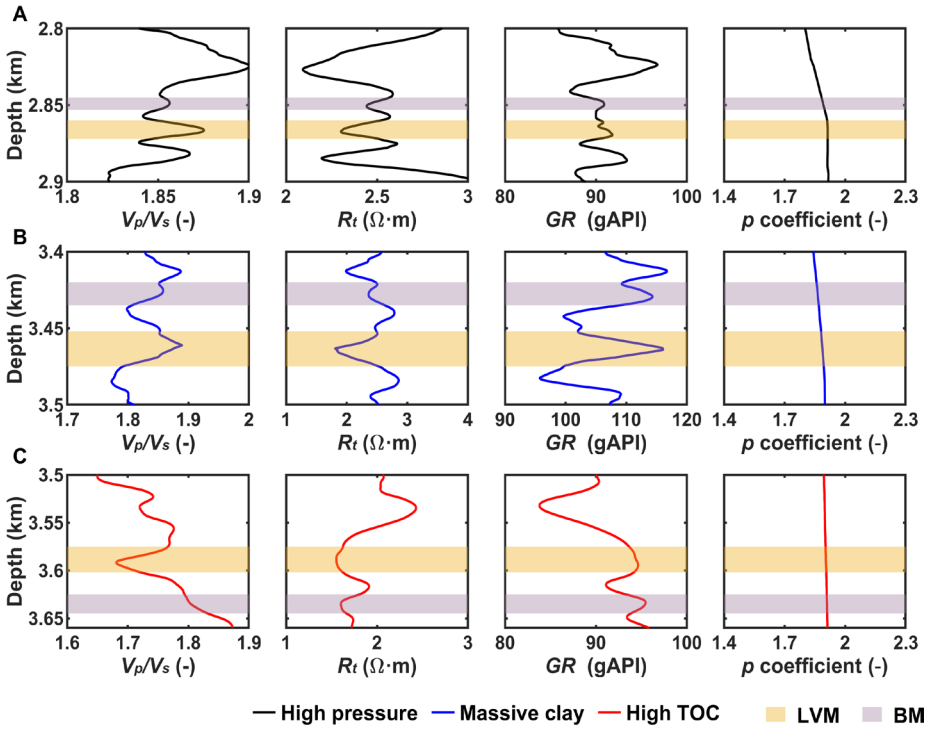

Figure 3. P- and S-wave velocity ratio (V_p/V_s), resistivity (R_t), gamma ray (GR), and pore pressure (p) coefficient that incorporates the data in Table 1. (A) First category of LVM. (B) Second category of LVM. (C) Third category of LVM.
Abbreviations: BM: Background mudstones; LVM: Low-velocity mudstone; TOC: Total organic carbon.

Figure 4A illustrates the correlation between V_p and clay content in Well A, revealing two distinct trends in mudstone velocity at varying clay contents. Notably, LVM exhibits significantly lower V_p than BM at similar clay contents. In addition, red and blue solid scatters represent GS and water-bearing sandstone, respectively. Figure 4B shows the relationship between mudstone V_p and p. It indicates that, as the p coefficient increases, mudstone V_p decreases significantly.

Similarly, Figure 5A illustrates the correlation between V_p and clay content in Well B. While the LVM with high clay content exhibited a trend consistent with the BM, the LVM in this layer exhibited a significantly lower value V_p due to its higher clay content. This low velocity may be related to the higher clay content, whereby clay functions as a skeletal component and reduces V_p.[6,10] For LVM with high TOC, however, the relationship between velocity and clay content exhibited a distinct trend compared to that of high clay content. Their velocities were markedly lower than those of BMs with equivalent clay content. However, as illustrated in Figure 5B, the relationship between V_p and organic carbon content shows a clear decrease in velocity with increasing organic carbon content. The low velocity characteristics of high organic carbon are primarily induced by TOC enrichment. Conventional seismic inversion methods struggle to distinguish this type of mudstone from GS reservoirs.

Compared to clay minerals, organic matter (primarily kerogen) has physical properties characterized by a low bulk modulus, a low shear modulus, and a low density.[19] The target exploration area's reservoir minerals are predominantly quartz and clay. Geochemical analysis indicated that the organic matter consists primarily of immature kerogen. Mudstone has low porosity and permeability, with pore fluids consisting mainly of water and gas.

3.2. Key steps of rock physics modeling

Figure 6 illustrates the rock physics modeling workflow, accounting for the physical properties of kerogen. First, the elastic modulus of the sand–clay matrix was calculated using the Voigt–Reuss–Hill (VRH) averaging principle. Meanwhile, the rock–skeleton modulus for pores containing TOC was computed using the self-consistent approximations (SCA) theory. To ensure the low-frequency assumption, the SCA theory was not directly applied for TOC filling. Instead, the Ciz–Gassmann equation was used for solid replacement, incorporating TOC as a pore-filler

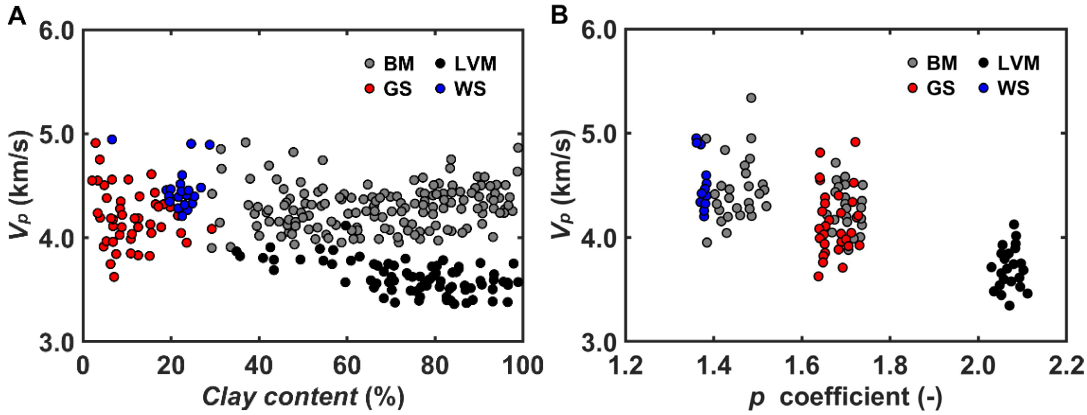

Figure 4. The relationship between (A) V_p and clay content, and (B) V_p and pore pressure coefficient of Well A
Abbreviations: BM: Background mudstone; GS: Gas-bearing sandstone; LVM: Low-velocity mudstone; WS: Water-bearing sandstone.

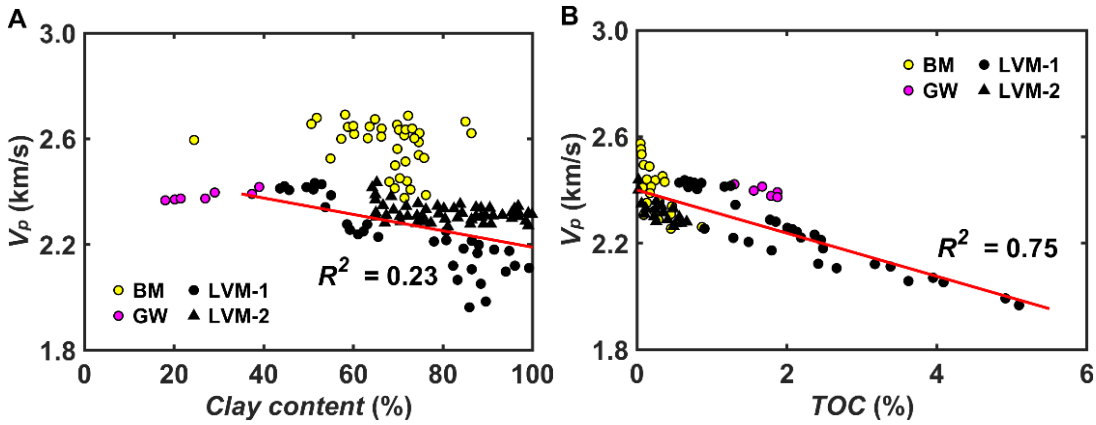

Figure 5. The relationship between (A) V_p and clay content, and (B) V_p and TOC of Well B
Abbreviations: BM: Background mudstone; GW: Gas-water-bearing sandstone; LVM: Low-velocity mudstone; TOC: Total organic carbon.

into the rock matrix to create a new equivalent matrix. Finally, SCA theory and the Gassmann equation were applied to calculate the elastic modulus of the equivalent matrix and the saturated rock. This ultimately yielded the V_p and V_s.

The elastic properties of saturated rocks are directly related to the rock matrix, rock skeleton, and fluid filling, and exhibit a nonlinear coupled relationship.[20–22] Seismic petrophysical modeling of LVM containing TOC involves five key steps that incorporate five fundamental petrophysical models: (i) the VRH average theory, (ii) the SCA model, (iii) the Ciz–Gassmann equation, (iv) the pore fluid modulus model, and (v) the Biot–Gassmann fluid replacement equation.

3.2.1. Rock matrix modulus

The elastic properties of rock are primarily contingent on the composition of the rock matrix, with the type and amount of diagenetic minerals present playing a pivotal role in determining the rock's specific elastic characteristics. In the field of rock physics, the VRH average model is typically employed to estimate the equivalent modulus of the rock matrix, which can be expressed as **Equation 1**[23]:

$$M_{\mathrm{m}} = \frac{1}{2}\left[\sum_{i=1}^{N} f_i M_i + \left(\sum_{i=1}^{N} f_i / M_i\right)^{-1}\right] \tag{1}$$

In the formula, M_{m} is defined as the equivalent bulk modulus, or shear modulus (K_{m}, G_{m}), of the matrix. M_i is expressed as the bulk modulus, or shear modulus (K_i, G_i), of the mineral components. f_i is represented as the content of the mineral components, and N is designated as the number of types of mineral components. The focus of this study is the exploration area, which primarily encompasses quartz and clay minerals, with $N = 2$.

3.2.2. Dry rock skeleton modulus

The porosity and pore structure of rock are significant factors in determining its elastic properties. The central theme of rock physics research is the establishment of a reasonable and equivalent description of the relationship

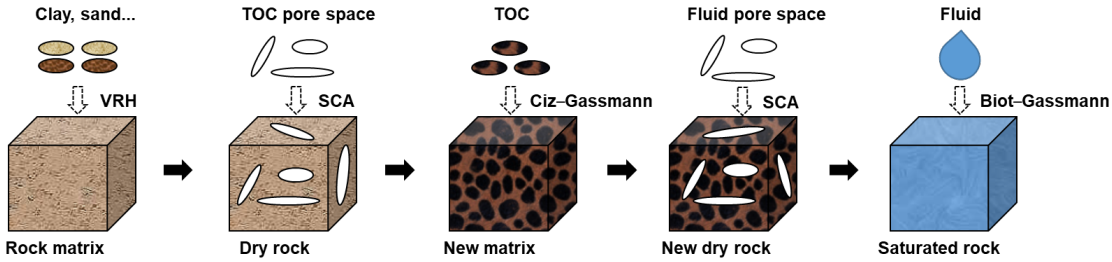

Figure 6. Rock physical modeling process of low-velocity mudstone containing TOC
Abbreviations: SCA: Self-consistent approximation; TOC: Total organic carbon; VRH: Voigt–Reuss–Hill.

between pore parameters and elastic parameters. In the context of the SCA theory, the porosity of the rock is equivalent to that of ellipsoids with a specific aspect ratio. Furthermore, the rock is equivalent to an equivalent medium composed of a matrix and inclusions with a particular aspect ratio. Therefore, the equivalent modulus of the rock skeleton can be calculated using the established method. The formula is expressed as **Equations 2** and **3**[24,25]:

$$\sum_{i=1}^{n} v_i \left(K_i - K_{\mathrm{SC}}^*\right) P^{*i} = 0 \tag{2}$$

$$\sum_{i=1}^{n} v_i \left(G_i - G_{\mathrm{SC}}^*\right) Q^{*i} = 0 \tag{3}$$

where n denotes the total number of inclusion types, v_i is the integral number of inclusion objects, and K_{SC}^* and G_{SC}^* are the equivalent bulk modulus and shear modulus, respectively. The coefficients P^{mi} and Q^{mi} are known as the polarization factors, defined as the effects of the i-th inclusion on the background matrix, respectively. K_i and G_i are the bulk modulus and shear modulus of the filler, respectively.

3.2.3. Solid substitution equations

In the case of the organic matter medium, which is characterized by its viscous properties, the solid substitution equations were employed to calculate the bulk modulus, denoted by K_{sat}, and the shear modulus, denoted by G_{sat}, when the pore space contains solids (**Equations 4** and **5**).[26]

$$K_{\mathrm{sat}}^{-1} = K_{\mathrm{dry}}^{-1} - \frac{\left(K_{\mathrm{dry}}^{-1} - K_{\mathrm{gr}}^{-1}\right)^2}{\phi\left(K_{if}^{-1} - K_{\phi}^{-1}\right) + \left(K_{\mathrm{dry}}^{-1} - K_{\mathrm{gr}}^{-1}\right)} \tag{4}$$

$$G_{\mathrm{sat}}^{-1} = G_{\mathrm{dry}}^{-1} - \frac{\left(G_{\mathrm{dry}}^{-1} - G_{\mathrm{gr}}^{-1}\right)^2}{\phi\left(G_{if}^{-1} - G_{\phi}^{-1}\right) + \left(G_{\mathrm{dry}}^{-1} - G_{\mathrm{gr}}^{-1}\right)} \tag{5}$$

It is imperative to note that K_{dry} and G_{dry} represent the bulk modulus and shear modulus of the dry rock skeleton, respectively, whereas K_{gr} and G_{gr} denote the bulk modulus and shear modulus of the background matrix, respectively. K_{if} and G_{if} are defined as the bulk modulus and shear modulus, respectively, with respect to the pore filler. K_{ϕ} and G_{ϕ} represent the pore-related bulk modulus and shear modulus, respectively. In accordance with the isotropic assumption, it can be demonstrated that $K_{\phi} = K_{\mathrm{gr}}$ and $G_{\phi} = G_{\mathrm{gr}}$.

3.2.4. Pore fluid modulus

The reservoirs within the exploration area consist of low-permeability clastic rocks, situated in the middle and deep layers. The pore structure is complex, and the gas–water immiscible fluid generally does not exhibit a highly relaxed, uniform filling state. A reasonable situation is that one fluid is filled into another fluid background in the form of patches, called the patch saturation state. The Brie model can be used to estimate the modulus of the mixed fluid (**Equation 6**)[27]:

$$K_{\mathrm{f}} = (K_{\mathrm{w}} - K_{\mathrm{hc}})(1 - S_{\mathrm{hc}})^e + K_{\mathrm{hc}} \tag{6}$$

where K_{w} and K_{hc} represent the bulk modulus of water and hydrocarbons, respectively. Furthermore, S_{hc} denotes hydrocarbon saturation, whilst e is an empirical constant that is contingent on the specific data under consideration.

3.2.5. Biot–Gassmann model

The medium under consideration is a fluid–solid two-phase medium. The Gassmann equation establishes the relationship among the rock matrix, fluid, and pore. To study the influence of fluid on the elastic properties of rock in the seismic frequency band, it is generally necessary to use the Gassmann equation to fill or replace the fluid. It has been demonstrated that the prediction result of the Gassmann equation is equivalent to the low-frequency limit of the Biot theory, and this result is known as the Biot–Gassmann model (**Equations 7** and **8**)[28]:

$$\tilde{K}_{\mathrm{sat}} = \tilde{K}_{\mathrm{dry}} + \alpha^2 \left[(\alpha - \phi)/K_{\mathrm{s}} + \phi/K_{\mathrm{f}}\right]^{-1} \tag{7}$$

$$\tilde{G}_{\text{sat}} = \tilde{G}_{\text{dry}} \tag{8}$$

where $\tilde{K}_{\text{sat}}$ and $\tilde{G}_{\text{sat}}$ are the bulk modulus and shear modulus of saturated rock, respectively. $\tilde{K}_{\text{dry}}$ and $\tilde{G}_{\text{dry}}$ represent the skeleton modulus of rocks filled with TOC, respectively. α is the Biot coefficient and $\alpha = 1 - \tilde{K}_{\text{dry}} / K_{\text{m}}$.

Following the acquisition of the modulus and density of saturated rock, the V_p and V_s of the rock medium can be calculated as in **Equations 9** and **10**:

$$V_p = \sqrt{\frac{\tilde{K}_{\text{sat}} + 4\tilde{G}_{\text{sat}}/3}{\rho_{\text{sat}}}} \tag{9}$$

$$V_s = \sqrt{\frac{\tilde{G}_{\text{sat}}}{\rho_{\text{sat}}}} \tag{10}$$

where ρ_{sat} denotes the saturated rock density.

3.3. Numerical simulation

To verify the rationality and applicability of the rock physics model developed in this study and to clarify the influence of parameters, such as organic matter content, clay content, and porosity, on the reservoir's elastic properties, a sand–mudstone forward simulation model was developed. The model under consideration was a sand–clay reservoir with TOC, with gas and water as the pore fluids. The TOC ranged from 1% to 6%, the porosity varied from 5% to 15%, and the clay content varied from 10% to 70%. As shown in Table 2, the fundamental parameters involved in the numerical example were derived from previous studies.[29–31]

Table 2. Numerical simulation parameters[29–31]

Parameters	Bulk modulus (GPa)	Shear modulus (GPa)	Density (g·cm^{-3})
Quartz	37	44	2.65
Clay	21	7	2.60
Total organic carbon	2.9	2.7	1.25
Water	2.5	0	1.03
Gas	0.00013	0	0.00065

When the clay content remained constant, adjustments were made to the TOC content and porosity. The outcomes of the elastic parameters simulated by the rock physics model are presented in Figure 7. It is evident that parameters such as V_p, V_s, V_p/V_s and P-wave impedance (PI) declined as TOC content increased. This is attributable to the lower bulk and shear moduli of TOC compared to those of sand and mud. The formation of TOC results in a reduction of the V_p and V_s of the reservoir. The V_p, V_s, V_p/V_s, and the PI decreased with increasing porosity. The presence of a low V_p/V_s and low PI may indicate the development of pores.

When porosity was held constant, and clay content and TOC were varied, the resulting elastic parameters predicted by the rock physics model are shown in Figure 8. It is evident that V_p, V_s, and PI decreased with an increase in clay content, while the V_p/V_s increased with increasing clay content. This indicates that V_p is more sensitive to changes in clay content, and the development of LVM may occur in layers with high V_p/V_s and low PI.

3.4. Inversion strategy

3.4.1. Core velocity inversion

The kerogen macerals in the core were identified, and the percentages of each maceral were quantified to determine the type of organic matter. The detection process was conducted using the fluorescence microscope (Axio Scope A1, ZEISS, Germany). Core samples from the survey area were obtained from qualified drilling. Figure 9 shows the kerogen macerals in the core samples at four depth points. According to the classification and analysis of organic matter types, the type index (TI) of sample A is −53.48, the TI of sample B is −57.35, the TI of sample C is −46.16, and the TI of sample D is −55.96, respectively. The detection results for the four samples showed that the kerogen type was type III.

Total organic carbon, V_p, and V_s measurements were also based on authentic samples. Table 3 lists the measurements for nine core samples. Prior to TOC determination, 100 mg of powder was meticulously weighed using an analytical balance. The samples were then immersed in a dilute hydrochloric acid solution (analytically pure) for at least 12 h. Thereafter, they were rinsed with deionized water to achieve neutrality. The samples were desiccated in an oven at 60 °C. The TOC of the samples was determined using a carbon–sulfur analyzer (CS744, LECO, America). The ultrasonic frequency band was used to measure both the longitudinal wave and shear wave velocities. The device under consideration consisted of a pulse generator, a digital oscilloscope, a longitudinal- and transverse-wave probe, a microcomputer, and a processing algorithm. The ultrasonic response of the core was measured using the transmission method, with a transducer frequency of 1,000 kHz. The crossplot of TOC with V_p, V_s, R_t, and V_p/V_s of nine core samples is shown in Figure 10. Testing results show that the V_p, V_s, R_t, and V_p/V_s decreased with increasing TOC, consistent with the rock physics modeling simulation conclusion.

Table 3. Total organic carbon (TOC), P-wave velocity (V_p),

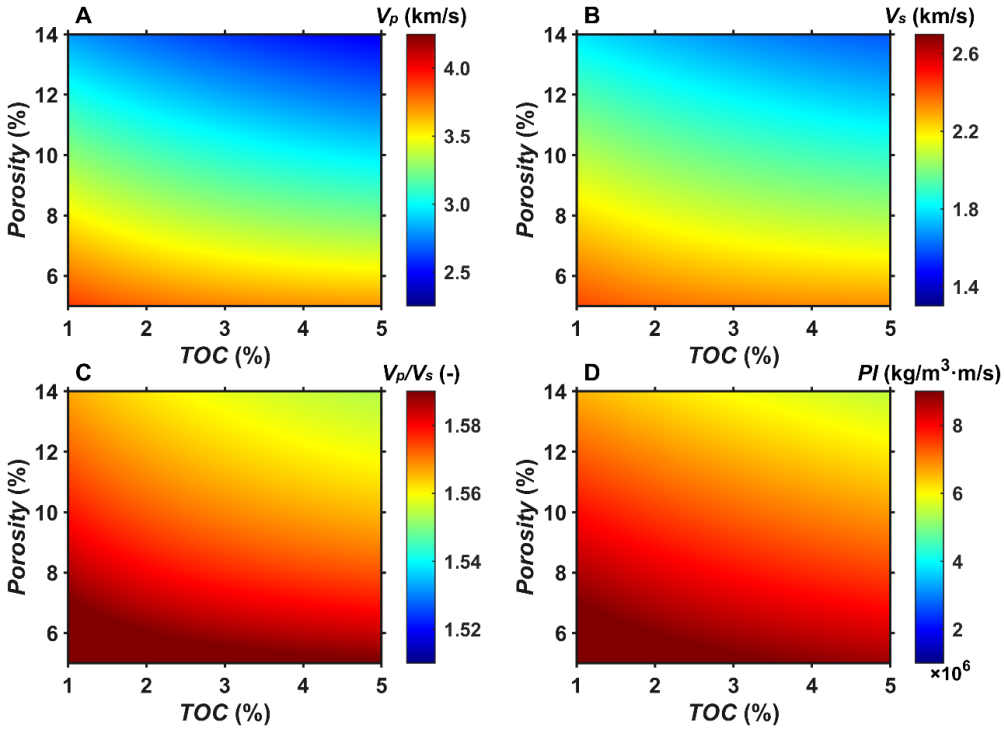

Figure 7. The variation of V_p, V_s, V_p/V_s and PI with TOC and porosity. (A) V_p with different TOC and porosity. (B) V_s with different TOC and porosity. (C) V_p/V_s with different TOC and porosity. (D) PI with a different TOC and porosity.
Abbreviations: PI: P-wave impedance; TOC: Total organic carbon; V_p: P-wave velocity; V_s: S-wave velocity.

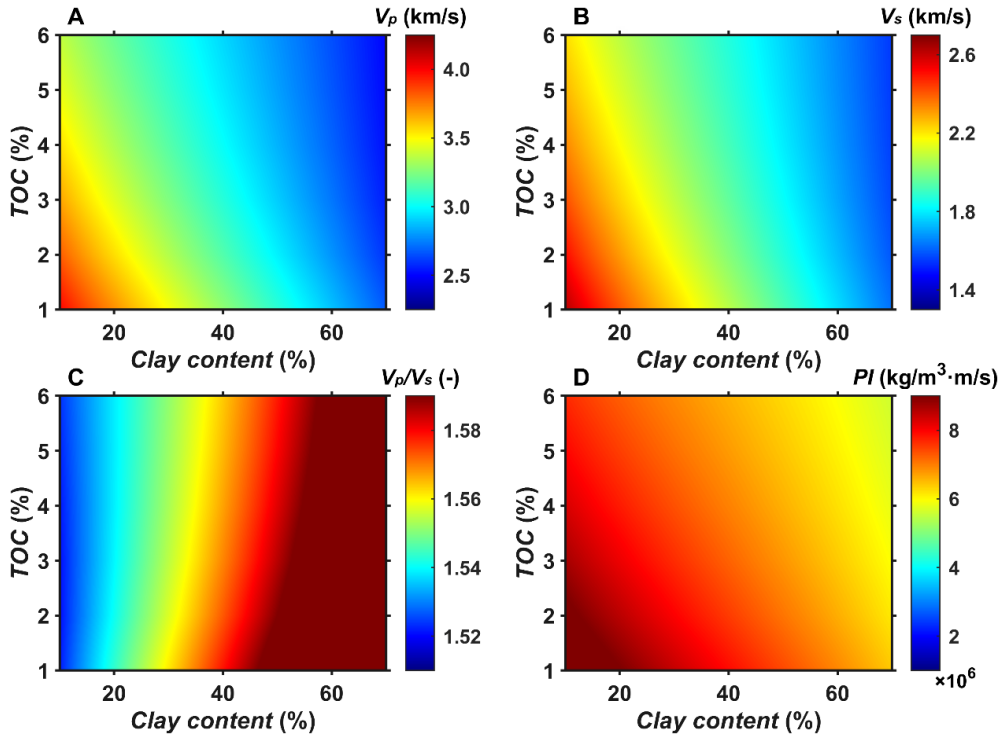

Figure 8. The variation of V_p, V_s, V_p/V_s and PI with clay content and TOC. (A) V_p with different clay content and TOC. (B) V_s with different clay content and TOC. (C) V_p/V_s with different clay content and TOC. (D) PI with different clay content and TOC.
Abbreviations: PI: P-wave impedance; TOC: Total organic carbon; V_p: P-wave velocity; V_s: S-wave velocity.

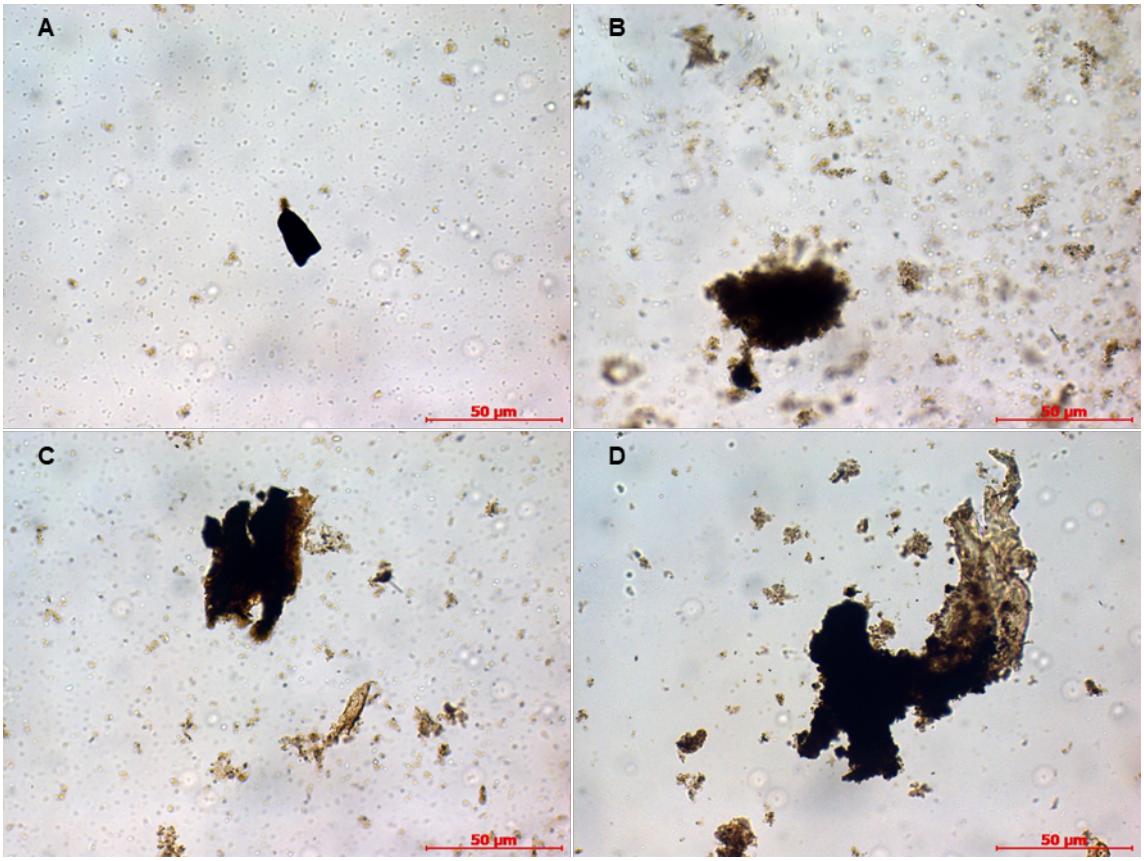

Figure 9. Micrograph images of kerogen macerals of four wall core samples from the survey area. (A) Mudstone of the borehole core sample, measured depth at 3,402 m. (B) Mudstone of borehole core sample, measured depth at 3,595 m. (C) Mudstone of borehole core sample, measured depth at 3,769 m. (D) Mudstone of the borehole core sample, measured depth at 3,897 m. Scale bar: 50 μm; magnification: 500×.

and S-wave velocity (V_s) data based on authentic core samples

Core sample	TOC (%)	V_p (m/s)	V_s (m/s)
C-1	1.17	3,119	1,696
C-2	5.67	2,959	1,687
C-3	2.95	3,562	1,989
C-4	3.50	3,249	1,770
C-5	0.41	3,699	2,206
C-6	0.63	3,685	1,993
C-7	2.09	3,471	1,785
C-8	1.00	3,161	1,587
C-9	1.59	2,930	1,604

The velocities of the nine samples were predicted to assess the validity of the aforementioned rock physics modeling method. As illustrated in Figures 11 and 12, the predicted and actual velocities were compared, with or without TOC. The ordinate denotes the predicted velocity, while the abscissa represents the actual velocity. It is evident that in the absence of kerogen, the predicted V_p and V_s exhibited higher than the actual velocities. Conversely, the predicted results that account for TOC showed greater alignment with the actual values.

3.4.2. Logging velocity inversion

The rationality of the rock physics model developed in this study was verified using actual logging data of Well X in an exploration area. Inversion of V_s can be defined as a nonlinear optimization problem. It is evident that simulated annealing is a reliable nonlinear inversion method.[32–35] In the current study, the actual velocity $\tilde{V}_p$, inverted velocity V_p, actual $\tilde{V}_p/\tilde{V}_s$ and inverted V_p/V_s were used to develop the inversion objective function as $g = \arg\min\left(\left\|\tilde{V}_p - V_p\right\|_2 + \left\|\tilde{V}_p/\tilde{V}_s - V_p/V_s\right\|_2\right)$. The V_s was calculated by inversion and compared with the measured velocity to evaluate the rationality of inversion and the effectiveness of the rock physics model. To predict inversions, it is necessary to consider several factors, including logging data and rock physical properties. The logging process involves measuring and interpreting parameters such

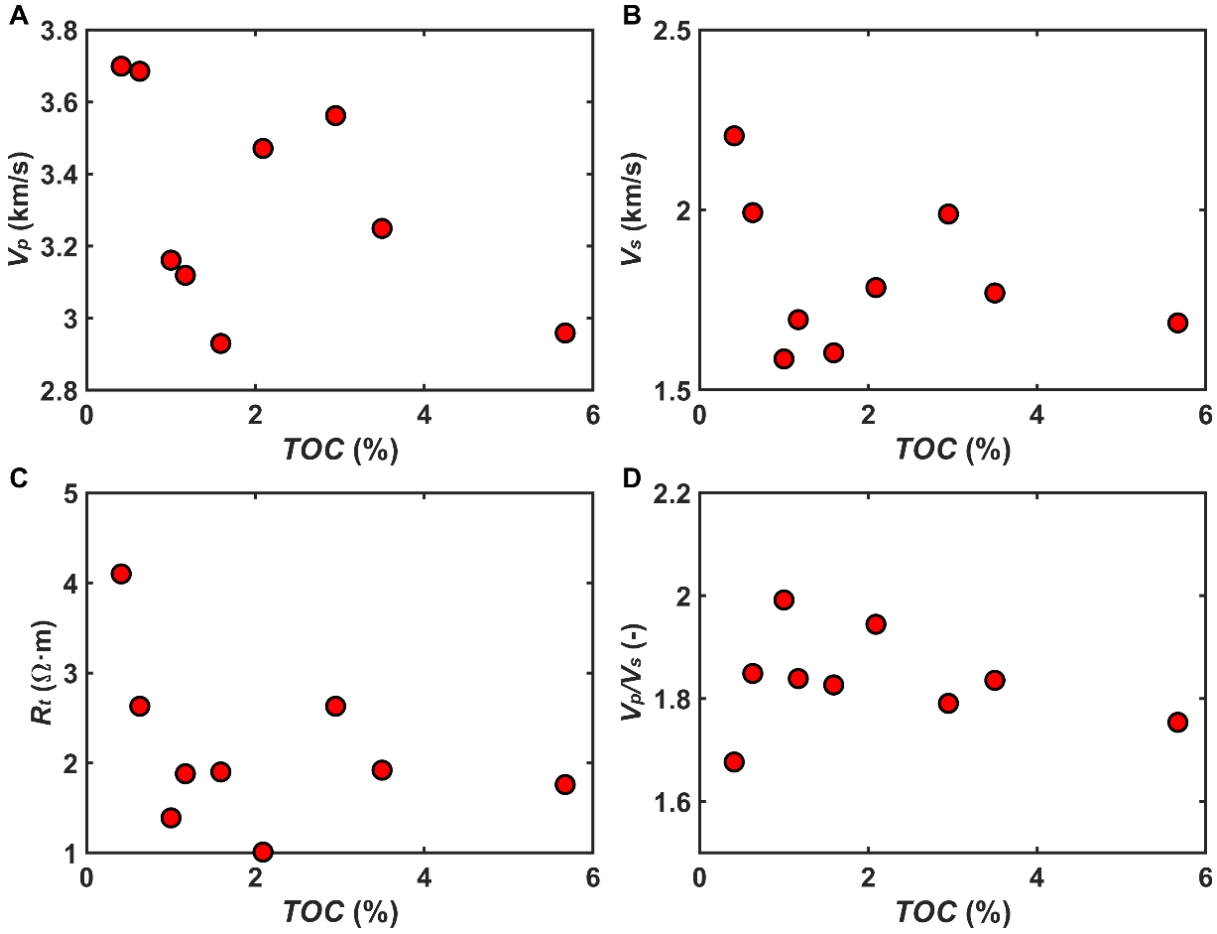

Figure 10. The cross-plots of the TOC with V_p, V_s, R_t, and V_p/V_s. (A) TOC and V_p. (B) TOC and V_s. (C) TOC and R_t. (D) TOC and V_p/V_s. Abbreviations: R_t: Resistivity; TOC: Total organic carbon; V_p: P-wave velocity; V_s: S-wave velocity.

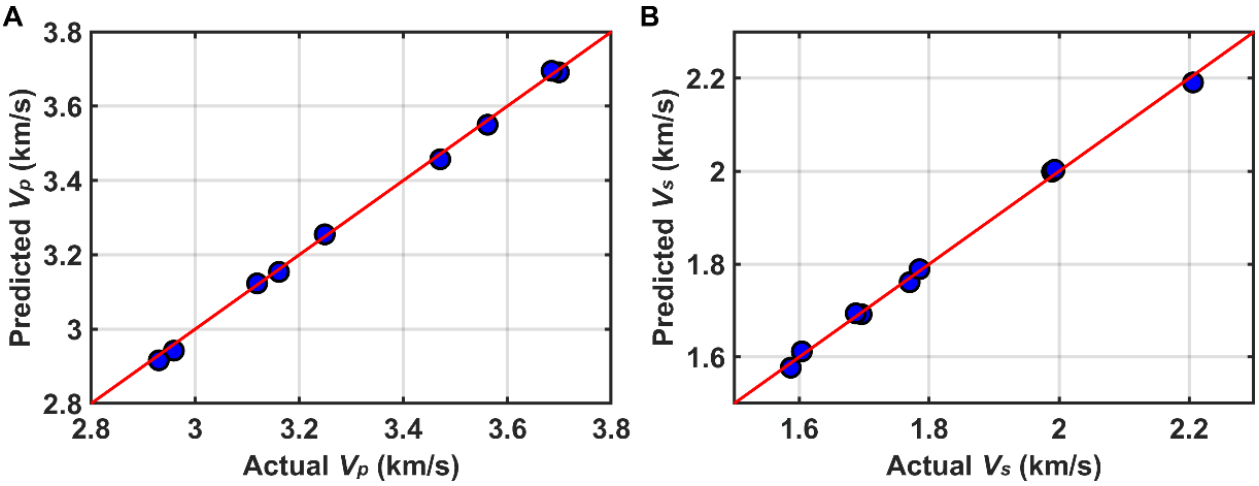

Figure 11. The cross-plots of the actual and predicted (A) V_p and (B) V_s
Abbreviations: V_p: P-wave velocity; V_s: S-wave velocity.

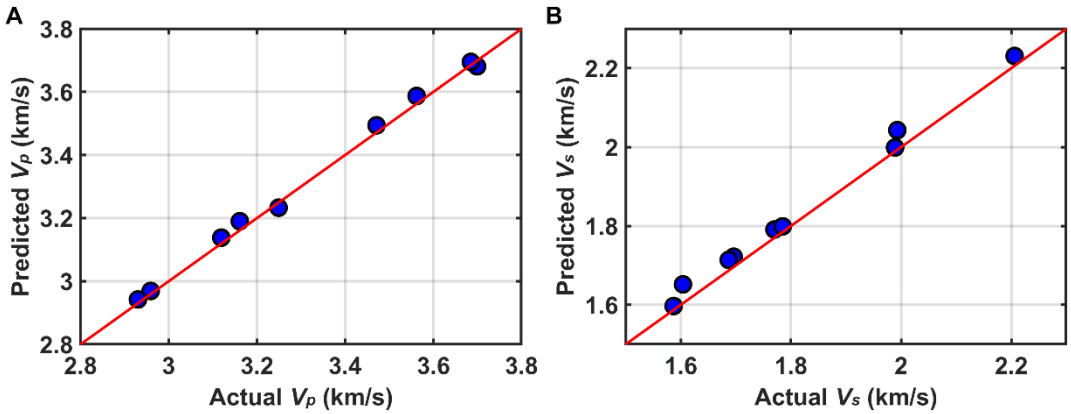

Figure 12. The cross-plots of the actual and predicted (A) V_p and (B) V_s, without the effect of total organic carbon
Abbreviations: V_p: P-wave velocity; V_s: S-wave velocity.

as mineral content, fluid saturation, porosity, and rock density.[36,37] These parameters can be obtained through direct measurement and logging interpretation. The logging data indicate that Well X was characterized by a medium-deep, low-porosity, and low-permeability clastic rock reservoir. The rock's mineralogical composition was dominated by quartz and clay, with occasional traces of calcite and mica. The porosity curve was interpreted from density logging data, while the saturation curve was calculated from resistivity logging data using the Archie formula. All interpretation conclusions were calibrated. The rock's physical parameters included the bulk modulus and shear modulus of each component, which were determined by the rock physical test results of the actual coring.

Figure 13 presents the comparison between the predicted and actual V_p and V_s in Well X. The lithology color marks—yellow and black—denote sandstone and mudstone, respectively. In the longitudinal and transverse wave curves, the ordinate denotes the depth, the abscissa signifies the velocity, the blue curve represents the inversion result, and the red curve corresponds to the measured velocity. Figure 14 presents the statistical analysis of inversion velocity error. The inversion V_p error was less than 5%, the V_s error was less than 10%, and the velocity error was small and generally presented a normal distribution also as shown in Figure 15. This indicates the applicability of the constructed rock physics model in the LVM formation in the exploration area.

The preceding analysis demonstrated the efficacy of the rock physics model in describing LVM containing organic matter, and the model-estimated elastic parameters were highly reliable.

4. Field examples

In the inversion strategy discussed in this study, the PI and velocity ratio were inverted using pre-stack seismic partial-stack gather data. This work was completed using the Jason software (version 24.2, GeoSoftware, USA). Prior to pre-stack inversion, it is imperative to preserve seismic data amplitude by applying fine-wavefront diffusion compensation, pre-stack denoising, and multiple removal, among other processes. Furthermore, it was assumed that the effects of interlayer multiples and anisotropy subsequent to processing can be disregarded. The wavelets used in the inversion were obtained via well-seismic calibration, and the low-frequency models were interpolated from well data.

For field seismic data from the Yinggehai Basin in the South China Sea, conventional pre-stack simultaneous inversion was previously regarded as a productive technique for differentiating sandstone and mudstone. However, implementing this strategy is challenging during the LVM development interval, which is characterized by the presence of organic matter. Figure 16 presents the seismic sections of the target area. Figure 16A–C corresponds to the 0–10°, 10–20°, and 20–30° (near, middle, and far) stack seismic sections, respectively.

The inversion results of PI and V_p/V_s are shown in Figure 17. Figure 17A,B represents the PI section and the V_p/V_s section, respectively. The red rectangular regions denote the GS, while the black rectangular region indicates the LVM layer.

It is noteworthy that in the inversion profiles of PI and the V_p/V_s, although the velocity ratio exhibited weaker lateral continuity compared to the impedance, distinct low-value

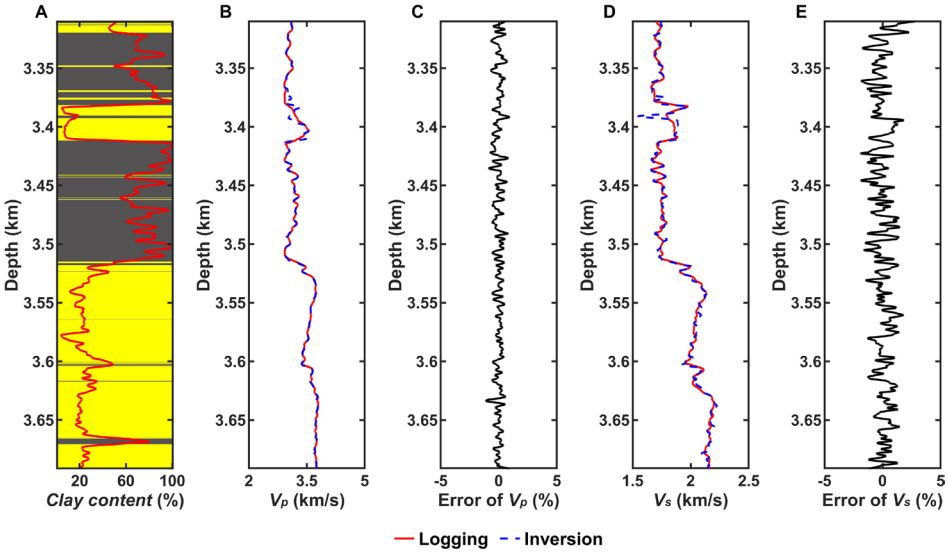

Figure 13. The comparison of the predicted and the actual V_p and V_s of Well X. (A) Lithology and clay content. (B) V_p of logging and inversion data. (C) Error of V_p. (D) V_s of logging and inversion data. (E) Error of V_s.
Abbreviations: V_p: P-wave velocity; V_s: S-wave velocity.

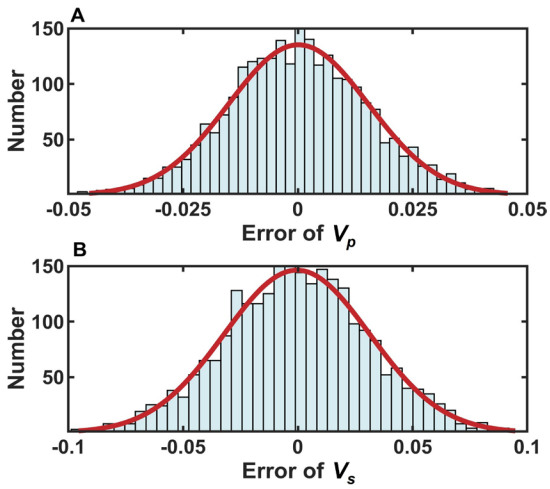

Figure 14. Error distribution between the measured and predicted (A) V_p and (B) V_s
Abbreviations: V_p: P-wave velocity; V_s: S-wave velocity.

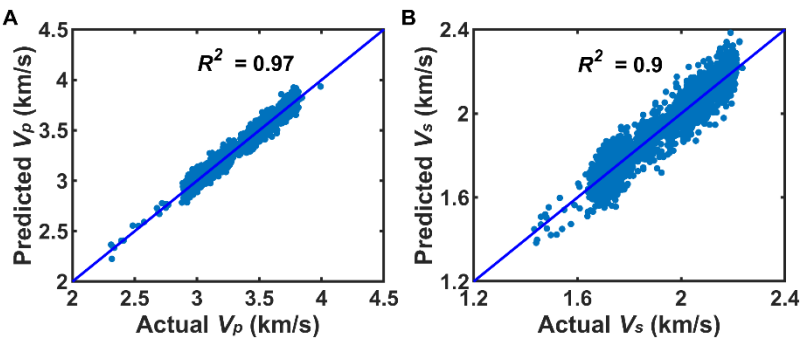

Figure 15. Cross-plots of the measured and predicted P and S wave velocities. (A) the V_p; and (B) the V_s .
Abbreviations: V_p: P-wave velocity; V_s: S-wave velocity.

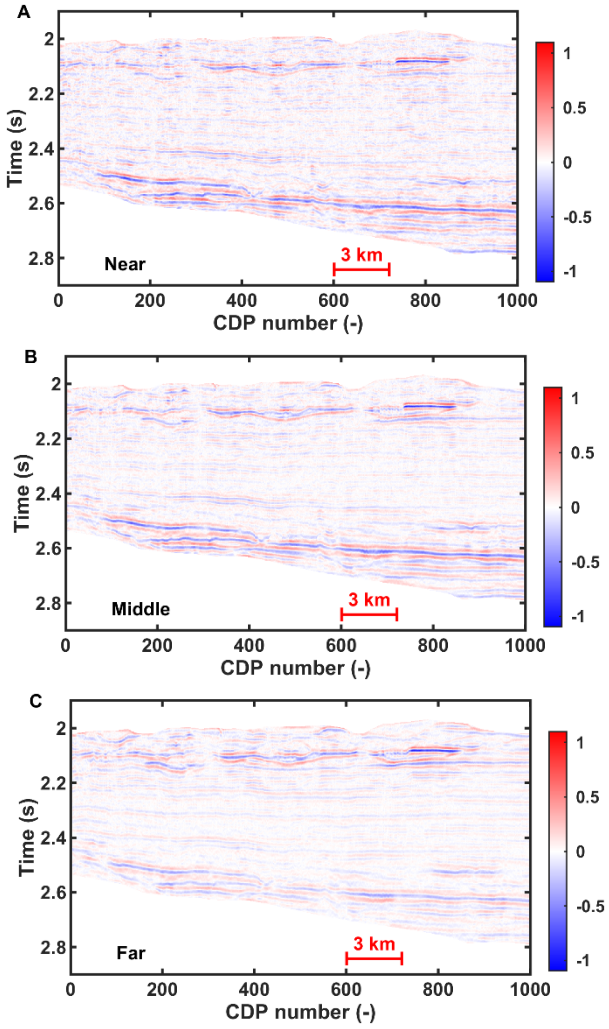

Figure 16. Partial angle stacking seismic profiles. (A) Near, stacking angles of 0–10°. (B) Middle, stacking angles of 10–20°. (C) Far, stacking angles of 20–30°.
Abbreviation: CDP: Common depth point.

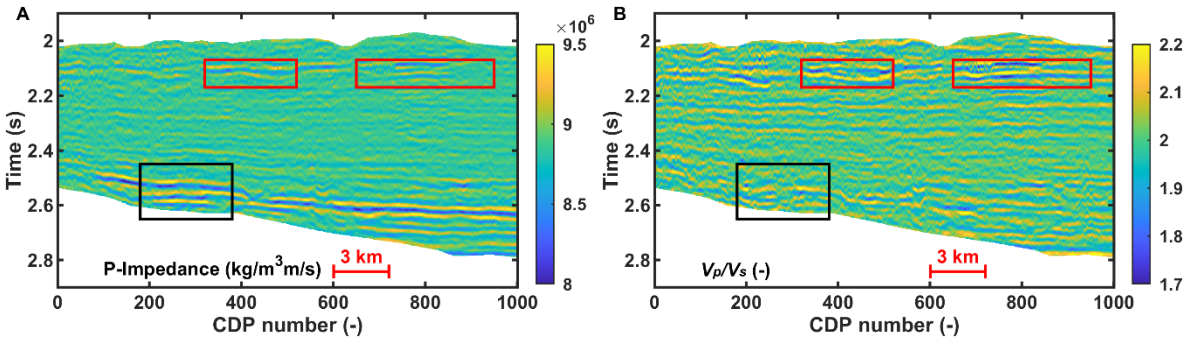

Figure 17. Pre-stack inversion results of elastic parameters. (A) P-impedance. (B) V_p/V_s.
Abbreviations: CDP: Common depth point; V_p: P-wave velocity; V_s: S-wave velocity.

anomalies can still be observed within the interval marked by the black rectangle. The consensus within the geophysical community is that impedance serves as an effective indicator for distinguishing sandstone from mudstone, while V_p demonstrates higher sensitivity to variations in gas saturation. Consequently, Figure 17 illustrates a key finding of this study that PI may misinterpret LVM as GS, and the low values present in the V_p/V_s profile further exacerbate this risk of misinterpretation. It is evident that all samples exhibited the characteristics of low PI and low V_p/V_s, which carries the potential risk of misinterpreting the LVM formation as GS.

In light of the aforementioned analysis and the novel rock physics model, the simulated annealing nonlinear inversion strategy was employed to facilitate the seismic inversion of petrophysical parameters for LVM reservoirs.[38–43] A well-connected line was selected, and the elastic parameters of the line were obtained by pre-stack inversion. These were then used as input data for physical parameter inversion. The initial inversion value was also generated by well interpolation, as shown in Figure 18. Inverted porosity, clay content, and water saturation are demonstrated in Figure 19. As shown in the seismic profile, there are strong-amplitude regions at travel times of 2.6 s and 2.1 s. It is challenging to circumvent LVM interference using conventional AVO attributes and pre-stack simultaneous inversion. As illustrated in Figure 19, the red rectangular regions denote the GS formation, while the black rectangular region indicates the LVM formation. The inversion results indicate that both porosity and gas saturation were elevated near 2.1 s, while there was an absence of discernible gas-bearing anomalies in the LVM section near 2.6 s. The inversion results provide a superior reflection of the actual drilling understanding, circumvent the LVM risk associated with conventional elastic parameters when predicting gas-bearing sweet spots, and facilitate the decoupling of GS and LVM.

The reliability of the inversion process can be evaluated by extracting the beside-borehole trace data from the inversion results and comparing them with the actual well data. Figure 20 compares the inversion results with the true values of porosity, clay content, and gas saturation. The reliability of the prediction results obtained using the rock physics model and inversion strategy in our study is well supported. The findings of this study demonstrate that, in the absence of consideration for the evident anisotropy, the petrophysical parameters of the formation can be reasonably inverted by employing the rock physics modeling and seismic inversion method delineated in this study. This is because the mudstone in the study area lacks a discernible directional arrangement of cracks or laminae, thereby allowing the influence of anisotropy on velocity to be reasonably ignored.[44]

5. Discussion

It is considered reliable for identifying sandstone and mudstone using rock physics intersection analysis and pre-stack simultaneous inversion. Moreover, it can be used to identify GS and dry sandstone. However, the petrophysical superposition of mechanism-containing LVM and GS in the Yinggehai Basin is significant, and the interpretation scheme for elastic parameters increases the risk of misjudgment of LVM as GS.

The organic matter content of mudstone significantly influences its elastic properties, thereby reducing its velocity. This effect is accompanied by a strong LVM amplitude, a phenomenon that cannot be disregarded in rock physics modeling. The establishment of a rock physics model for the LVM reservoir in the Yinggehai Basin is predicated on analysis of relevant geological data and seismic rock physics characteristics. The model was developed with consideration for the influence of TOC. The influence of TOC on seismic elastic properties was considered, and the contributions of TOC, porosity, and clay content to velocities were analyzed. The simulation demonstrated that the V_p, V_p/V_s, and PI decreased with an increase in TOC, thereby elucidating the microscopic rock-physics mechanism of mudstone low impedance anomaly.

Notably, although the content of organic matter in mudstone was higher, the overall content was lower than that of shale source rocks. In contrast to the substantial vertical transverse isotropy exhibited by shale, the organic-rich LVM predominantly manifested as a massive structure with minimal brittle mineral content. The fracturing process is challenging, and the current geological survey does not consider its horizon to be conducive to oil and gas reservoir formation. However, in this study, the viscosity of organic matter significantly affected the propagation velocity of seismic waves.

It is important to note that kerogen's viscosity can cause velocity dispersion and wave energy attenuation, leading to differences across acoustic, logging, and seismic frequency bands. The extant research demonstrates that the velocity of seismic waves in the low-frequency range is typically marginally lower than that of the logging and ultrasonic frequency bands. The associated modeling can account for wave-induced fluid flow mechanisms or viscoelastic mechanisms. However, when taken in conjunction with the Biot flow theory and squirt flow theory, the Biot attenuation peak of fast longitudinal waves will shift to the high frequency band with an increase in fluid viscosity, while the squirt flow attenuation peak will shift to the

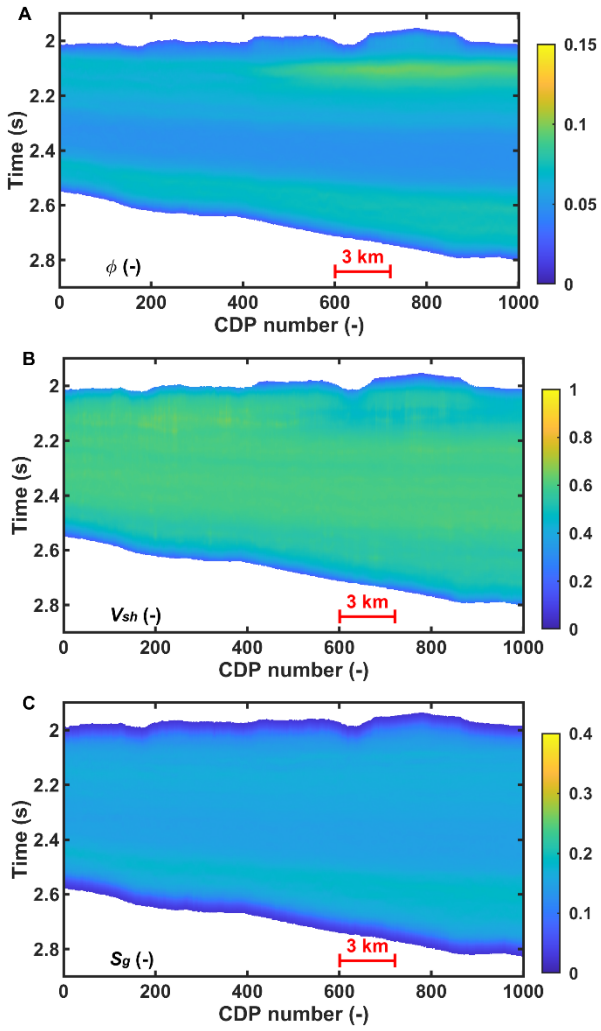

Figure 18. Initial model profile of (A) porosity (ϕ), (B) clay content (V_{sh}), and (C) gas saturation (S_g)
Abbreviation: CDP: Common depth point.

low frequency band with an increase in fluid viscosity. The incorporation of this attenuation mechanism into rock physics modeling introduces additional parameters, such as tortuosity and crack density. The accurate and precise articulation of these parameters is challenging. It is therefore evident that the modeling scheme described in this study is based on the equivalent medium theory, and the attenuation and dispersion of kerogen pairs can be discussed using multi-band rock physics experimental data.

As the elastic modulus of kerogen is considerably lower than that of background minerals such as quartz, in this study, kerogen and background minerals were not treated as equivalent to the background matrix. Rather, they were part of the pore filler, and their low-frequency characteristics were maintained. Organic matter may be found within micro-cracks, intergranular pores, or biological cavity pores. However, the development pattern of kerogen in rock media is more complex. Adsorption of organic matter on the surface and within the pores of mineral particles (particularly clay minerals) occurs in an amorphous form, constituting the primary manifestation of the dispersion pattern at the micro level. Under a microscope, kerogen and mineral particles were observed to be intermingled, forming an organic–mineral complex. This complicates the process of distinguishing individual kerogen particles, and the rock physics modeling method for this distribution pattern warrants further discussion in future work.

6. Conclusion

The seismic elastic characteristics of organic-rich LVM have

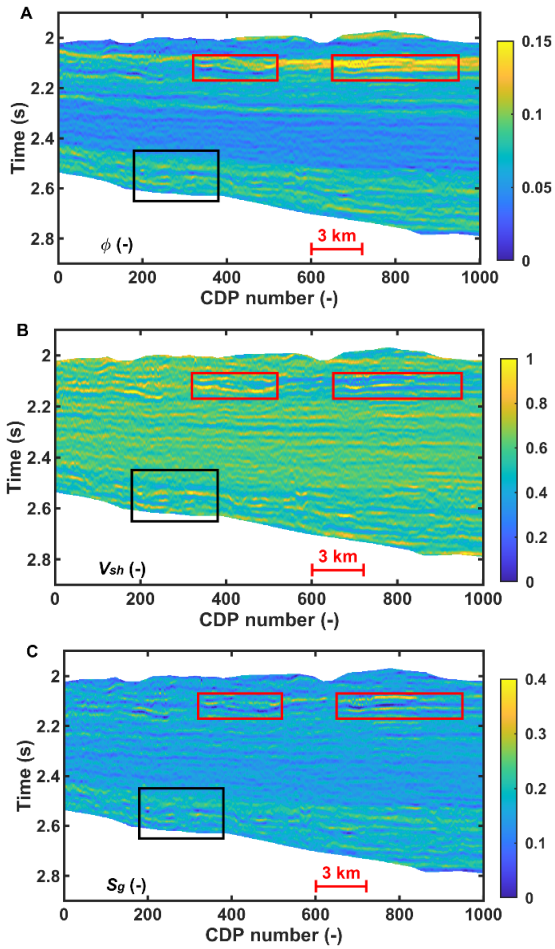

Figure 19. Profile of (A) porosity (ϕ), (B) clay content (V_{sh}) and (C) gas saturation (S_g) from inversion
Abbreviation: CDP: Common depth point.

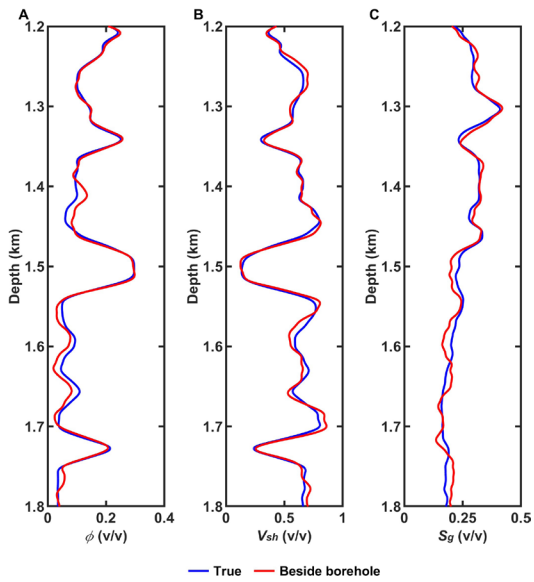

Figure 20. Comparison of the true data and the predicted borehole results of porosity ϕ, clay content V_{sh} and gas saturation S_g, for which the true data are in blue, and the predicted results are in red. (A) Porosity ϕ. (B) clay content V_{sh}. (C) gas saturation S_g.

been shown to be analogous to those of GSs. The presence of kerogen in the mudstone of the Yinggehai Basin has been demonstrated to be the cause of the pronounced amplitude observed. The present study used the rock physics modeling scheme of the SCA model and the Ciz–Gassmann equation to predict the V_p and V_s of LVM containing organic matter. This theoretical foundation facilitates the identification of LVM through seismic inversion. The methodology employed was founded on the principles of rock physics, specifically the V_p and V_s equations. This approach enables the robust inversion of porosity, clay content, and saturation. The subsequent data processing serves to validate the method's viability for practical applications and, concurrently, provides a seismic inversion method for identifying GS and LVM from seismic data. The method was applied to the exploration target, enabling quantitative seismic predictions of porosity, clay content, and saturation using a rock physics model. The inversion results were in good agreement with the drilling results, which verifies the effectiveness of the method. In the context of reservoir seismic identification, it is imperative to enhance the precision of inversion predictions by leveraging seismic and logging data alongside the evaluation of formation lithology. Consequently, it is imperative to establish a direct relationship between the seismic reflection coefficient and the physical parameters in subsequent work. Moreover, developing a rational pre-stack direct inversion method is essential to eliminate cumulative error in indirect inversion. This will facilitate a more effective execution of reservoir seismic identification and evaluation.

Acknowledgments

The authors express their gratitude to Dr. Kun Lang, Dr. Songhe Yu, and Professor Shiyou Liu for their discussions.

Funding

This study was financially supported by the National Oil and Gas Major Project of China, "Amplitude preserving imaging technology with high precision and multiple geophysical field exploration technology for deep-water complex geological conditions in South China Sea" (Grant No. 2025ZD1402706).

Conflict of interest

The authors declare that they do not have any commercial or associative interest that represents a conflict of interest in connection with the work submitted.

Author contributions

Conceptualization: Jinpeng Li, Yanhua Xie
Formal analysis: Yanhua Xie, Jinpeng Li, Wanyuan Sun
Investigation: Yanhua Xie, Wanyuan Sun, Yayun Dang
Methodology: Jinpeng Li, Yanhua Xie, Fang Li
Visualization: Yanhua Xie, Wanyuan Sun
Writing–original draft: Yanhua Xie, Wanyuan Sun
Writing–review & editing: Yanhua Xie, Jinpeng Li, Yayun Dang

Availability of data

The data in this paper is subject to the following licenses/restrictions: National confidential data. Requests to access these datasets should be directed to the corresponding author.

References

1. Guo XX, Hu L, Wu YY, Xiong XF, Yu HW, Xia L. Gas generation potential of Oligocene source rocks in Yinggehai Basin. *Nat Gas Ind B*. 2024;11(6):728-738.

   doi: 10.1016/j.ngib.2024.11.006

2. Pei JX, Yu JF, Wang LF, Hao DF, Liu F. Key challenges and strategies for the success of natural gas exploration in mid-deep strata of the Yinggehai Basin. *Acta Pet Sin*. 2011;32(4):573-579. [in Chinese].

   doi: 10.7623/syxb201104003

3. Wu KQ, Pei JX, Hu L, Hu GW, Tang SM, Zhao H. Accumulation model and exploration direction of medium-large gas fields in Yinggehai Basin. *Acta Pet Sin*. 2023;44(12):2200-2216. [in Chinese].

   doi: 10.7623/syxb202312012

4. Zhang XY, Fan CW, Alves TM, *et al*. Hydrocarbon generation in source rocks with low organic matter as the primary mechanism for overpressure development: A case study from the Yinggehai Basin, South China Sea. *J Geol Soc*. 2025;183(1):jgs2024-157.

   doi: 10.1144/jgs2024-157

5. Xie YH, Li XS, Tong CX, Liu P, Wu HZ, Huang ZL. High temperature and high pressure gas enrichment condition, distribution law and accumulation model in central diaper zone of Yinggehai basin. *China Offshore Oil Gas*. 2015;27(4):1-12. [in Chinese].

   doi: 10.11935/j.issn.1673-1506.2015.04.001

6. Yang GX, Yin HW, Jia D, Wang HB, Wang W, Xu WQ. New insights into the structure of the Yinggehai Basin and its tectonic implications, South China Sea: Evidence from scaled physical models. *Basin Res*. 2024;36(4):e12888.

   doi: 10.1111/bre.12888

7. Xie YH, Gao YD. Recent domestic exploration progress and direction of CNOOC. *China Pet Explor*. 2020;25(1):20-30.

[in Chinese].

doi: 10.3969/j.issn.1672-7703.2020.01.003

8. Xie YH. China National Offshore Oil Corporation: Major achievements in oil and gas exploration of CNOOC in the 13th Five-Year Plan period and prospects in the 14th Five-Year Plan period. *China Pet Explor.* 2021;26(1):43-54. [in Chinese].

doi: 10.3969/j.issn.1672-7703.2021.01.004

9. Tong CX, Wang ZF, Li XS. Pooling conditions of gas reservoirs in the Dongfang 1-1 Gas Field, Yinggehai Basin. *Nat Gas Ind.* 2012;32(8):11-15. [in Chinese].

doi: 10.3787/j.issn.1000-0976.2012.08.003

10. Li F, Deng Y, Hu L, Zhou F. Porosity prediction by geophysics technology at low-porosity and low-permeability reservoir of the Yinggehai Basin. *Bull Geol Sci Technol.* 2022;41(4):84-90. [in Chinese].

doi: 10.19509/j.cnki.dzkq.2021.0060

11. Grana D, Rossa ED. Della Rossa E. Probabilistic petrophysical-properties estimation integrating statistical rock physics with seismic inversion. *Geophysics*. 2010;75(3):O21-O37..

doi: 10.1190/1.3386676

12. Russell BH, Gray D, Hampson DP. Linearized AVO and poroelasticity. *Geophysics*. 2011; 76(3):C19-C29.

doi: 10.1190/1.3555082

13. Yin XY, Cui W, Zong ZY, Liu XJ. Petrophysical property inversion of reservoirs based on elastic impedance. *Chin J Geophys.* 2014;57(12):4132-4140. [in Chinese].

doi: 10.6038/cjg20141224

14. Zong ZY, Yin XY, Wu GC. Fluid identification method based on compressional and shear modulus direct inversion. *Chin J Geophys*. 2012;55(1):284-292. [in Chinese].

doi: 10.6038/j.issn.0001-5733.2012.01.028

15. Luo C, Ba J, Guo Q. Probabilistic seismic petrophysical inversion with statistical double-porosity Biot-Rayleigh model. *Geophysics*. 2023; 88(3):M157-M171.

doi: 10.1190/geo2022-0288.1

16. Li K, Yin X, Zong Z. Facies-constrained prestack seismic probabilistic inversion driven by rock physics. *Sci China Earth Sci*. 2020;63(6):822-840.

doi: 10.1007/s11430-019-9578-1

17. Ba J, Ai ZJ, Carcione JM, Pang MQ, Yan XF, Chen X. Estimation of pore structure for heterogeneous reservoirs based on the theory of differential poroelasticity. *Pure Appl Geophys.* 2024, 181(7):2131-2147.

doi: 10.1007/s00024-024-03510-3

18. Li H, Zhang J, Pan H, Gao Q. Nonlinear simultaneous inversion of pore structure and physical parameters based on elastic impedance. *Sci China Earth Sci*. 2021;64(6):977-991.

doi: 10.1007/s11430-020-9773-8

19. Carcione JM. A model for seismic velocity and attenuation in petroleum source rocks. *Geophysics*. 2000;65(4):1080-1092.

doi: 10.1190/1.1444801

20. Zhang GZ, Chen JJ, Chen HZ, Ma ZG, Li CC, Yin XY. Prediction for in-situ formation stress of shale based on rock physics equivalent model. *Chin J Geophys.* 2015;58(6):2112-2122. [in Chinese].

doi: 10.6038/cjg20150625

21. Ba J, Xu W, Fu LY, Carcione JM, Zhang L. Rock anelasticity due to patchy-saturation and fabric heterogeneity: A double-double porosity model of wave propagation. *J Geophys Res Solid Earth.* 2017;122(3):1949-1976..

doi: 10.1002/2016JB013882

22. Dutilleul J, Bourlange S, Géraud Y, Stemmelen D. Porosity, pore structure, and fluid distribution in the sediments entering the northern Hikurangi margin, New Zealand. *J Geophys Res Solid Earth*. 2020;125(11):1-21. .

doi: 10.1029/2020JB020330

23. Hill R. The elastic behavior of crystalline aggregate. *Proc Phys Soc.* 1952;65(5):349-354.

doi: 10.1088/0370-1298/65/5/307

24. Berryman JG. Long-wavelength propagation in composite elastic media I. Spherical inclusions. *J Acoust Soc Am.* 1980;68(6):1809-1819.

doi: 10.1121/1.385171

25. Berryman JG. Long-wavelength propagation in composite elastic media II. Ellipsoidal inclusions. *J Acoust Soc Am*. 1980;68(6):1820-1831.

doi: 10.1121/1.385172

26. Ciz R, Shapiro SA. Generalization of Gassmann's equations for porous media saturated with a solid material. *Geophysics*. 2007;72(6):A75-A79.

doi: 10.1190/1.2772400

27. Brie A, Pampuri F, Marsala AF, Meazza O. Shear sonic interpretation in gas-bearing sands. In: *SPE Annual Technical Conference and Exhibition*. SPE Annual Technical Conference and Exhibition; October 22–25, 1995; Dallas, Texas. Society of Petroleum Engineers (SPE); 1995.

doi: 10.2118/30595-ms

28. Gassmann F. Elastic waves through a packing of spheres. *Geophysics*. 1951;16(4):673-685.

doi: 10.1190/1.1437718

29. Yu SH, Zong ZY, Li K. Rock physics and seismic reflectivity parameterization for amplitude-variation-with-angle inversion of low-maturity source rocks. *Geophysics*. 2023;88(6):R703-R719.

doi: 10.1190/geo2022-0734.1

30. Zong ZY, Yu SH, Tan H, Yin XY, Li K. Nonlinear seismic inversion of total organic carbon for hydrocarbon source rocks. *Geophysics*. 2025;90(5):MR375-MR390.

doi: 10.1190/geo2024-0288.1

31. Zhao LX, Qin X, Han DH, Geng JH, Yang ZF, Cao H. Rock-physics modeling for the elastic properties of organic shale at different maturity stages. *Geophysics*. 2016;81(5):D527-D541.

doi: 10.1190/geo2015-0713.1

32. Zhang JJ, Li HB, Yao FC. Rock critical porosity inversion and S-wave velocity prediction, *Appl Geophys*. 2012;9(1):57-64.

doi: 10.1007/s11770-012-0314-8

33. Yang YH, Yin XY, Gao G, Gui ZX, Zhao B. Shear-wave velocity estimation for calciferous sandy shale formation. *J Geophys Eng.* 2019;16(1):105-115.

doi: 10.1093/jge/gxy009

34. Wang JL, Wu SG, Zhao LX, Wang WW, Wei JG, Sun J. An effective method for shear-wave velocity prediction in sandstones. *Mar Geophys Res*. 2019;40(4):655-664.

doi: 10.1007/s11001-019-09396-4

35. Zhang L, Ba J, Carcione JM, Wu CF. Seismic wave propagation in partially saturated rocks with a fractal distribution of fluid-patch size. *J Geophys Res Solid Earth*. 2022;127(2):e2021JB023809.

doi: 10.1029/2021JB023809

36. Pang MQ, Ba J, Carcione JM, Picotti S, Zhou J, Jiang R. Estimation of porosity and fluid saturation in carbonates from rock-physics templates based on seismic Q. *Geophysics*. 2019;84(6):M25–M36.

doi: 10.1190/geo2019-0031.1

37. Yin XY, Zong ZY, Wu GC. Research on seismic fluid identification driven by rock physics. *Sci China Earth Sci.* 2015;58(2):159-171.

doi: 10.1007/s11430-014-4992-3

38. Chapman S, Tisato N, Quintal B, Holliger K. Seismic attenuation in partially saturated Berea sandstone submitted to a range of confining pressures. *J Geophys Res Solid Earth*. 2016;121(3):1664-1676.

doi: 10.1002/2015JB012575

39. Bosch M, Mukerji T, Gonzalez EF. Seismic inversion for reservoir properties combining statistical rock physics and geostatistics: A Review. *Geophysics*. 2010;75(5):A165-A176.

doi: 10.1190/1.3478209

40. Zhu DH, Gibson R. Seismic inversion and uncertainty quantification using transdimensional Markov Chain Monte Carlo method. *Geophysics*. 2018;83(4):R321-R334.

doi: 10.1190/geo2016-0594.1

41. Kolbjørnsen O, Arild B, Ragnar H, Per R, Abel Onana N, Eyvind A. Bayesian seismic inversion for stratigraphic horizon, lithology, and fluid prediction. *Geophysics*. 2020;85(3):R207-21.

doi: 10.1190/geo2019-0170.1

42. Wang C, Yin C, Shi XW, *et al*. Direct prediction method of fracturing ability in shale formations based on pre-stack seismic inversion. *J Seism Explor.* 2022;31(5):407-424.

43. Zhou XY, Gan LD, Yang TQ, Jiang XY, Wei LL. S-wave velocity estimation and reservoir type identification based on partially connected porosity model of carbonate reservoir. *J Seism Explor*. 2023;32(1):51-65.

44. Sharifi J, Amiri M, Fakhar M, Hafezi Moghaddas N. An experimental study on variation of pore pressure and wave velocity in carbonate rocks: impact of depositional facies and diagenesis. *Geomech Geophys Geo-Energy Geo-Resour.* 2026;12(8):1-31.

doi: 10.1007/s40948-025-01062-x